

Lignin Laser Lithography: A Direct-Write Method for Fabricating 3D Graphene Electrodes for Microsupercapacitors

Wenli Zhang, Yongjiu Lei, Fangwang Ming, Qiu Jiang, Pedro M. F. J. Costa, and Husam N. Alshareef*

In this work, a simple lignin-based laser lithography technique is developed and used to fabricate on-chip microsupercapacitors (MSCs) using 3D graphene electrodes. Specifically, lignin films are transformed directly into 3D laser-scribed graphene (LSG) electrodes by a simple one-step CO₂ laser irradiation. This step is followed by a water lift-off process to remove unexposed lignin, resulting in 3D graphene with the designed electrode patterns. The resulting LSG electrodes are hierarchically porous, electrically conductive (conductivity is up to 66.2 S cm⁻¹), and have a high specific surface area (338.3 m² g⁻¹). These characteristics mean that such electrodes can be used directly as MSC electrodes without the need for binders and current collectors. The MSCs fabricated using lignin laser lithography exhibit good electrochemical performances, namely, high areal capacitance (25.1 mF cm⁻²), high volumetric energy density (≈1 mWh cm⁻³), and high volumetric power density (≈2 W cm⁻³). The versatility of lignin laser lithography opens up the opportunity in applications such as on-chip microsupercapacitors, sensors, and flexible electronics at large-scale production.

The rapid development of miniaturized electronic devices, such as micro-electromechanical systems, wireless sensors, implantable medical devices, and microrobots, has stimulated the need for miniaturized energy storage devices.^[1,2] Compared with microbatteries, microsupercapacitors (MSCs) have attracted much attention for miniaturized energy storage due to their long lifespan, high reversibility, and high power densities.^[3,4] Over the past decades, great efforts have been made in the fabrication, miniaturization, and integration of MSCs.

Generally, MSCs are fabricated into in-plane interdigitated electrodes through complex photolithography technique

inspired by the fabrication technology used in the semiconductor industry. The electrode materials of MSCs can be prepared by various, well-developed techniques, such as inkjet printing,^[5–8] screen printing,^[9,10] electrophoretic deposition,^[11] electrodeposition,^[12,13] and laser scribing.^[14,15] Compared with other techniques, laser scribing technology is a simple direct-write method that does not require photolithography masks or tedious multistep fabrication processes.^[16–23] In previous studies, graphene films were prepared from hydrated graphene oxide (GO) through laser scribing technology,^[14,24] where GO could be reduced to rGO through the laser scribing process. However, the preparation of GO is complicated and time consuming. A more simple and direct approach is laser-scribing polyimide, which was developed by Tour and co-workers who fabricated laser-scribed graphene (LSG) electrodes from commercial Kapton polyimide film.^[15] Different from thermal carbonization method, the laser scribing carbonization of polyimide provides LSG with highly porous graphene structure and high conductivity. Since then, LSG has been used in microsupercapacitor,^[25–30] electrocatalytic hydrogen generation,^[31,32] electrochemical oxygen evolution,^[33] sensors,^[34–36] and antimicrobial applications.^[37,38] Recently, Tour and co-workers have done some excellent work that extended the laser scribing technology to wood and several polymers to make porous graphene films.^[37,39] Polysulfone-class polymers have been transformed into graphene by one-step laser scribing, and various natural products, textile fabrics, and even bread have been transformed into graphene by multiple-laser-scribing technology.^[40]

As one of the three ingredients of natural biomass (lignin, cellulose, and hemicellulose), lignin is the most abundant renewable natural aromatic polymer existing in the world. Lignin is a kind of phenylpropane-based complex reticular aromatic polymer and cannot be utilized by traditional chemical-engineering routes. Most existing lignins are extracted by sulfite pulping in the paper industry as a by-product pollutant in “black liquor.” As a result, lignin is usually considered to be useless and even as an environmental contaminant. Thus, the transformation of

Dr. W. L. Zhang, Y. J. Lei, F. W. Ming, Q. Jiang, Prof. P. M. F. J. Costa, Prof. H. N. Alshareef
Materials Science and Engineering
Physical Sciences and Engineering Division
King Abdullah University of Science and Technology (KAUST)
Thuwal 23955-6900, Saudi Arabia
E-mail: husam.alshareef@kaust.edu.sa

The ORCID identification number(s) for the author(s) of this article can be found under <https://doi.org/10.1002/aenm.201801840>.

DOI: 10.1002/aenm.201801840

lignin into high-value-added products has both scientific and commercial significance for the sustainable development of society.^[41,42] Lignin should be a good carbon precursor since it has numerous aromatic rings. However, most lignin-derived carbons have been amorphous carbons up to now.^[43–45] Tour and co-workers used alkali lignin as precursor to prepare LSG, but they only got high viscous materials.^[39] Although various lignin-containing natural materials can be transformed into LSG via multistep lasing technique,^[40] the production of LSG from pure lignin has not been realized. The transformation of lignin into graphene could therefore realize large-scale and low-cost production of graphene. In this study, we have successfully prepared high-quality LSG from lignin films by one-step lasing technique. We also developed a lignin-based laser lithography process and used it to fabricate on-chip MSCs with excellent performance. The lignin-based laser lithography allows the free fabrication of MSCs with various electrode materials using a simple water-based lift-off process.

The details of our lignin laser lithography (LLL) process are shown in **Figure 1**. First, a lignin/polyvinyl alcohol (PVA) composite film was prepared by blade-coating a lignin/PVA

solution (10 wt%) on the ozone-treated polymer substrate (Figure 1, step 1). After drying, lignin/PVA film was exposed to CO₂ laser to convert the exposed regions into comb-like interdigitated electrodes (Figure 1, step 2 and step 3). The geometric size and structure of the MSC are shown in Figure S1 in the Supporting Information. Our process then takes advantage of the fact that alkaline lignin can be dissolved in water, as shown in Figure 1, step 4. Basically, a water lift-off process is used to remove the parts of the lignin film that were not exposed to the laser. This step leaves the designed patterned electrode structure on the surface of the substrate. Since we can pattern any active shape on the substrate using both laser and water-soluble lignin, the combined role of lignin and laser makes a facile lithography technique, which we name LLL.

Digital photos of LSG electrode patterns fabricated by LLL technique on various substrates are shown in Figure S2 in the Supporting Information. Specifically, Figure S2A in the Supporting Information shows the black electrodes formed from Lignin /PVA film on polycarbonate (PC) substrate. Before the water lift-off process, the patterned black graphene electrodes are surrounded by brownish lignin/PVA unexposed to the

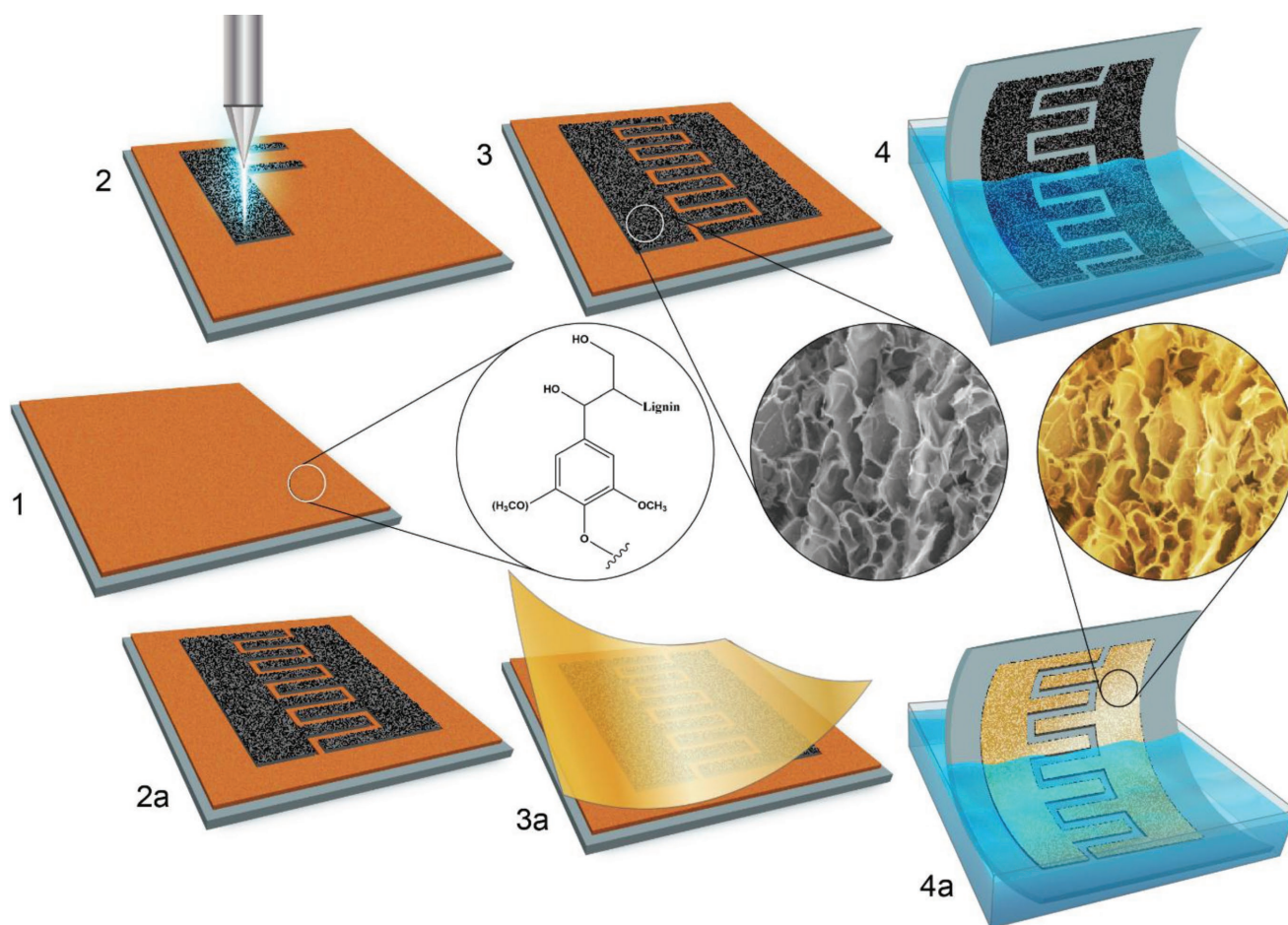


Figure 1. Schematic diagram of the lignin laser lithography (LLL) technique. 1) Preparation of lignin/PVA film on substrate by blade coating technique, the blow up of 1 shows the typical unit structure of lignin. 2) Laser scribing process for the preparation of LSG from lignin film. 3) The laser-scribed graphene MSC pattern. 4) Water lift-off to remove unexposed lignin film to finish the lignin laser lithography process. 2a) The laser-scribed graphene MSC patterns before Au coating. 3a) Sputtered Au coating on LSG-based finger electrodes. 4a) Water lift-off to remove lignin film unexposed to laser to finish the lignin lithography process.

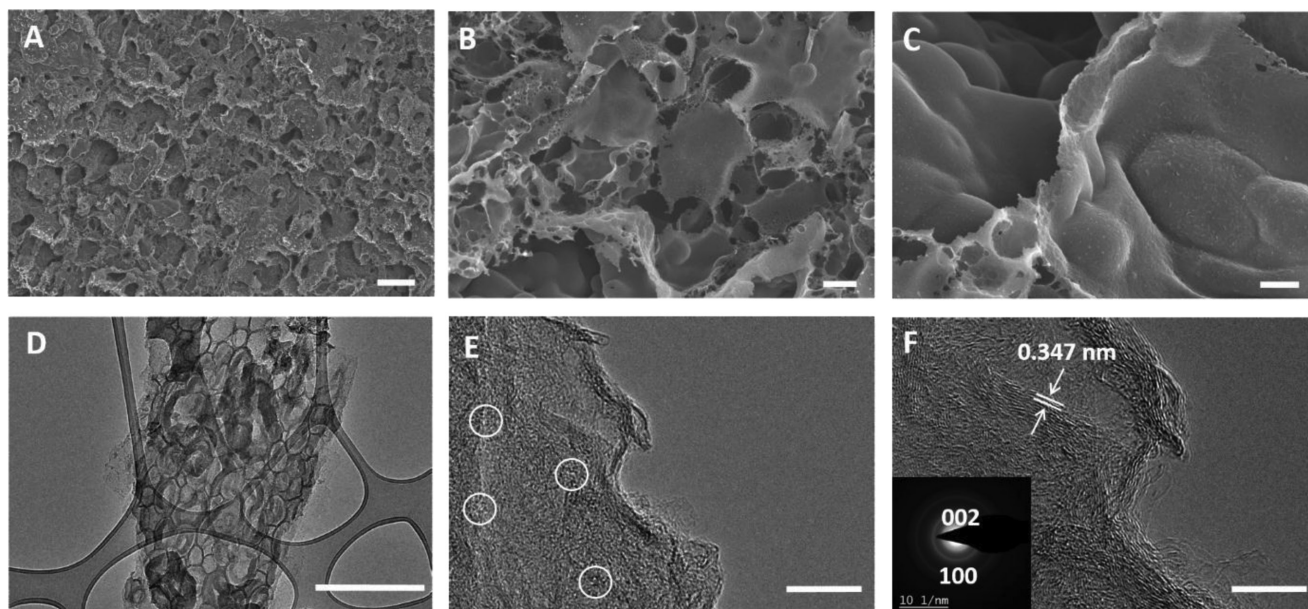


Figure 2. The surface morphology and inner structure of LSG electrode scribed using 3.6% laser power (LSG-P36). A) The SEM image of LSG-P36, scale bar is 10 μm , B,C) the high resolution SEM images of LSG-P36, scale bars are 1 μm and 500 nm, respectively, D) TEM images of LSG-P36, scale bar is 500 nm, and E,F) HRTEM image of LSG-P36, scale bars are 20 and 10 nm, respectively. The white circles in (E) show some typical nanopores inside the carbon matrix of LSG-P36. The inset of (F) shows the corresponding SAED pattern.

laser. However, after soaking the sample in water, the lignin/PVA film unexposed to laser was removed. The resulting electrode pattern is shown in Figure S2B in the Supporting Information. Similarly, Figure S2C,D in the Supporting Information shows the compatibility of our lithography process with other common polymer substrates, including poly(methyl methacrylate) (PMMA) (Figure S2C, Supporting Information) and polyethylene terephthalate (PET) (Figure S2D, Supporting Information). In addition, the LLL method can be applied to make many types of patterns as shown in Figure S2E in the Supporting Information (KAUST and its logo were patterned by LLL on PET substrate).

The LLL technique can be extended to make more complex multilayered electrodes consisting of various materials deposited on LSG (such as metals and metal oxides) to improve supercapacitor performance or to enable other applications. This approach is shown in Figure 1 which illustrates how this concept can be used to make Au/LSG electrodes using LLL. Basically, after exposing lignin to the laser and conversion from lignin to LSG (Figure 1, step 2a), one could coat the LSG electrode with another active material before the water lift-off process. Figure 1, step 3a, shows that an Au coating was deposited to increase the conductivity of the LSG electrodes. Following the Au coating, the device was soaked in water which resulted in the lift-off of lignin and Au in the areas where lignin was not exposed to laser. As a result, an Au/LSG bilayer electrode with designed pattern remained after the water lift-off of lignin. An actual device with Au/LSG electrodes fabricated using the LLL process is shown in Figure S2F in the Supporting Information. This approach can in principle be extended to other material/LSG electrode combinations other than Au/LSG. For example, common supercapacitor materials including oxide/LSG, sulfide/LSG, and polymer/LSG can be fabricated using LLL.

It is interesting to note that LSG electrodes derived from lignin show similar morphology to LSG electrodes derived from polyimide (see the scanning electron microscopy (SEM) in Figure 2A). The morphology of LSG electrodes obtained with a 3.6% laser power (denoted as LSG-P36) is shown in Figure 2B,C. The observed coarse morphology with numerous embedded macropores results from the release of gaseous products (H_2O , CO_2 , etc.) upon the total decomposition of PVA (Figure S3, Supporting Information) and the partial decomposition of lignin during the laser scribing process.^[15,46] These large, numerous macropores were also found in the transmission electron microscopy (TEM) images (Figure 2D). The high-resolution TEM (HRTEM) image of LSG-P36 shows that some fine nanosized pores also exist inside the electrodes (Figure 2E). The above results demonstrate that the lignin-derived LSG electrodes have 3D hierarchical porous structures composed of macropores and nanosized pores. The nanosized pores could increase the electrochemically active surface area, while macropores could facilitate the electrolyte diffusion, which should be beneficial for electrochemical microsupercapacitor performance.

The evolution of morphology and porous structure with laser power were studied by SEM and TEM. With the increase of laser power from 2.4% to 3.2%, the surface of LSG evolves from closed-pore morphology to opened-pore morphology (Figure S4A–C, Supporting Information). With further increase of laser power to 3.6% and 4.0%, some parts of the LSG film were detached from the surface due to the highly oxidizing atmosphere (Figure S4D,E, Supporting Information). A laser power higher than 4.0% will destroy the continuity of LSG film. High-resolution SEM images shown in Figure S5 in the Supporting Information display some small bright particles on the surface of LSGs, and these particles seem to protrude from

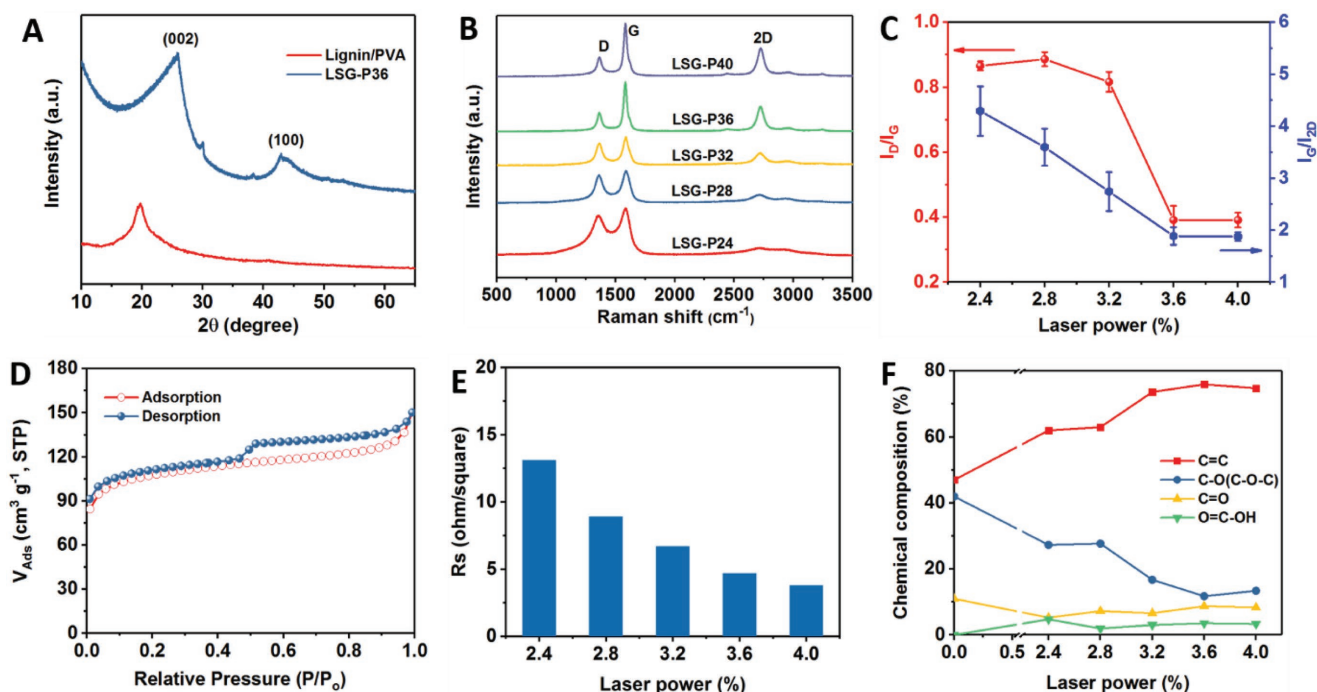


Figure 3. Physicochemical properties of lignin-derived LSGs. A) The XRD patterns of lignin/PVA and LSG electrode prepared at 3.6% laser power (LSG-P36). B) Raman spectra of LSG electrodes prepared at different laser power. C) The dependence of I_D/I_G and I_D/I_{2D} ratios on laser power. D) N_2 adsorption–desorption curves of the LSG-P36 electrode. E) The sheet resistances of LSGs prepared at different laser power. F) Chemical compositions of LSG electrodes derived from the fitting of C 1s spectra of lignin/PVA and the LSGs at different laser powers.

the surface with increasing laser power. These particles actually are Na_2SO_4 particles originating from the decomposition of sodium sulfonate in alkaline lignin and the crystallization of small Na_2SO_4 crystals. These particles can be easily washed off during the water lift-off process as demonstrated by the SEM images of the water-washed LSGs in Figure S6 in the Supporting Information. The formation of Na_2SO_4 demonstrates that the laser-scribing formation of LSG is a combined photochemical and photothermal process.^[46]

The HRTEM images show that LSG-P36 possesses long graphene layers with a lattice space of about 0.347 nm (Figure 2F), corresponding to the distance between two neighboring (002) planes in graphitic carbons. Two dominant peaks in selected area electron diffraction (SAED) pattern indexed to (002) and (100) planes suggest the existence of scrolled or folded graphene in LSG. The above results show that during the laser scribing process, lignin has been successfully transformed into 3D hierarchical porous graphene. The inner structures of LSGs were further characterized via TEM upon the change of laser power (Figure S7, Supporting Information). All the low magnification TEM images show macroporous structure and the HRTEM images show nanosized pores, which demonstrates that our lignin-derived LSG is indeed a hierarchical porous carbon. An interesting phenomenon is that the content of nanosized pore decreases with increasing laser power (Figure S7F–J, Supporting Information). This effect could be explained by the fact that the carbon radicals, generated from the breaking of carbon–carbon bonds^[46] during laser scribing, tend to combine together to form well-crystallized graphene layers and do not form pores at higher laser power. As a result, with the

increase of laser power, clear evolution of the formation of graphitic structures in LSG can be observed. For the LSG-P32 electrode (lased at 3.2% laser power), some short-range graphene domains can be found, while when the laser power increased to 3.6% (LSG-P36), clearly stacked, long graphene layers can be seen (Figure S7, Supporting Information).

The graphitic structure of LSGs was also demonstrated by X-ray diffraction (XRD) (Figure 3A). The intense XRD peak of LSG-P36 centered at $\approx 25.9^\circ$ can be assigned to (002) reflection giving an interlayer spacing of 0.344 nm, which is consistent with the TEM results. The asymmetry of the (002) peak demonstrates that some disordered amorphous structure exists in the LSG structure. Raman spectra of the lignin-derived LSG electrodes show three dominating peaks (Figure 3B): the D peak (K-point phonons of A_{1g} symmetry) at 1360 cm^{-1} , induced by the defects in LSG; the G peak (E_{2g} phonons of C sp^2 atoms) at 1570 cm^{-1} and 2D peak at 2700 cm^{-1} , originating from the second order zone-boundary phonons.^[47] When lignin was irradiated at a laser power of 2.0% or below, neither G nor D peak was observed. However, when laser power increased to 2.4%, lignin started to transform into low-graphitic carbon, as suggested by the broad D peak and the weak 2D peak. The decreased D peak intensity and increased G and 2D peak intensities were observed when the laser power increased from 2.8% to 4.0%, which demonstrates the formation of higher quality graphitic structure. The Raman spectra were further analyzed and summarized in Figure 3C. The lowest I_D/I_G ratio (0.39) was obtained when the applied laser power increased to 3.6%, which means that the crystallite size of graphene is the largest (L_a is 30.7 nm) (Figure S8, Supporting Information). The LSG-P36

electrode also shows the smallest I_G/I_{2D} ratio, indicating the stacking of the fewest number of graphene layers. These results suggest that higher laser power generally leads to the formation of higher quality graphene.^[40]

The specific surface area and inner porous structure of LSG were characterized by N_2 adsorption–desorption analysis (Figure 3D). The isotherm of LSG-P36 is a combined I/IV type according to the International Union of Pure and Applied Chemistry (IUPAC) classification, indicating that numerous mesopores and micropores exist in the carbon skeleton. According to the Brunauer–Emmett–Teller (BET) model, LSG-P36 electrode has a BET surface area of $338.3 \text{ m}^2 \text{ g}^{-1}$. The total pore volume of LSG-P36 is $0.232 \text{ cm}^3 \text{ g}^{-1}$ with an average pore diameter of 2.57 nm (Table S1, Supporting Information), which is very similar to LSG derived from polyimide.^[15] Besides, LSG-P36 has some mesopores larger than 20 nm (Figure S9, Supporting Information). The mesopores combined with the large macropores in LSG form a 3D hierarchical porous structure, which is beneficial for supercapacitor performance. The large macropores facilitate electrolyte diffusion, while the small nanosized pores act as active sites for electrical double layer capacitor (EDLC).

Besides the hierarchical porous structure, LSG also has high conductivity. The sheet resistance of LSG decreased with increasing laser power (Figure 3E). Below the threshold power of 2.4%, lignin is an insulator. With the increase of laser power, the sheet resistance decreased from 13.1Ω per square of LSG-P24 to 3.8Ω per square of LSG-P40. The conductivity of LSG increased with the increase of laser power. The LSG-P24 sample has a conductivity of 19.1 S cm^{-1} , while LSG-P40 has a high conductivity of 66.2 S cm^{-1} (Figure S10, Supporting Information).

The chemical composition of LSGs was analyzed by X-ray Photoelectron spectroscopy (XPS) as shown in Figure S11 in the Supporting Information. The C 1s peaks were fitted into four components (Figure S12, Supporting Information), including the $\text{sp}^2 \text{ C}=\text{C}$ bond located around 284.4 eV, the C–O bond located around 285.7 eV, the C=O bond located around 288.5 eV, and C(O) O bond located around 290.5 eV. Figure 3F shows that the concentration of $\text{sp}^2 \text{ C}=\text{C}$ bonds increased with increasing laser power and stabilized at around 75% for laser power of 3.6%. The XPS results suggest that LSGs are dominated by sp^2 carbons, agreeing well with the TEM, XRD, and Raman results. In contrast, the concentration of the C–O bonds decreased with increasing laser power. The increase of $\text{sp}^2 \text{ C}=\text{C}$ bond with increasing CO_2 laser power is expected to increase the conductivity of LSG, as shown in Figure S10 in the Supporting Information. Owing to the relatively low content of $\text{sp}^2 \text{ C}=\text{C}$ bond in LSG-P24 and LSG-P28, they exhibit lower conductivity. As a summary, the laser scribing of lignin not only carbonized lignin (Figure S13, Supporting Information) but also led to the formation of porous LSG with high graphitic carbon content and high conductivity.

As discussed above, lignin-derived LSGs have high conductivity, hence can be used directly as the electrode active materials of MSC without the need for binders and current collectors. On the other hand, the highly porous structure of LSG can provide MSC with high capacitance. The electrochemical performance of LSG MSCs having interdigital electrodes fabricated using our LLL technique are shown in Figure 4. It can be seen that LSG electrodes fabricated using various laser

powers all show symmetric quasi-rectangular C–V curves indicating fast EDLC type charge storage mechanism (Figure 4A). From Figure 4A, we can deduce that LSG-P24 possesses the highest areal capacitance among LSGs at a scan rate of 0.1 V s^{-1} , which could be attributed to the high nanopore density in the carbon matrix (Figure S7, Supporting Information). Quasi-rectangular C–V curves of LSG-P24 at different scan rates demonstrate good EDLC behavior (Figure 4B). The dependence of areal capacitance of LSG electrodes on applied laser power is plotted in Figure 4C, at different scan rates. The fastest capacitance decay with scan rate (lowest rate capability) is observed for the LSG-P24 device, which could be due to the high equivalent series resistance (ESR) of LSG-P24 (Figure S14, Supporting Information) and high density of small nanosized pores (Figure S7, Supporting Information). The ESRs for LSG-P24, LSG-P28, LSG-P32, LSG-P36, and LSG-P40 MSCs are 30, 24, 14, 8.6, and 8.5Ω , respectively, whose tendency is consistent with the four-point probe resistance test. It can be seen that the areal capacitance of LSG decreases with increasing applied laser power. The LSG-P24 electrodes exhibit the highest areal capacitance (15.4 mF cm^{-2}) while the LSG-P40 electrodes exhibit the lowest areal capacitance (3.0 mF cm^{-2}) at a scan rate of 0.01 V s^{-1} . On the other hand, the LSG-P28, LSG-P32, and LSG-P36 electrodes show comparable but decreasing areal capacitance (areal capacitance is 7.0, 6.0, and 5.5 mF cm^{-2} , respectively). The decreasing areal capacitance of LSGs with increasing laser power results from both the lower nanosized pore density in the carbon matrix (Figure S7, Supporting Information) and the detachment of some carbon from LSG surface at higher laser power ($\geq 3.6\%$, Figure S4, Supporting Information).

The charge–discharge (CD) curves of LSG electrodes prepared at different laser power are all fairly symmetric and triangular in shape (Figure 4D), indicating good capacitive behavior and high coulombic efficiency. The areal capacitance calculated from the CD curves for LSGs prepared at different laser powers are generally consistent with those obtained from the C–V curves (Figure 4C), where areal capacitance decreases with increasing laser power. The LSG-P24 electrodes show higher capacitance compared with those obtained from the cyclic voltammetry (CV) test due to the longer time in CD test. LSG-P24 shows a capacitance of 17.0 mF cm^{-2} (4.25 F cm^{-3} , in Figure S15A, Supporting Information) at a current density of 0.05 mA cm^{-2} , while the capacitance of LSG-P24 is 15.4 mF cm^{-2} at a scan rate of 0.01 V s^{-1} . Besides, LSG-P24 shows good EDLC behavior at different CD current densities (Figure 4D). The change of areal capacitance with laser power can also be revealed by the Nyquist plot. For instance, LSG-P24 shows a lower Z_{im} at 10 mHz compared with other LSG electrodes (Figure S14A, Supporting Information), which means that LSG-P24 possesses the highest capacitance.

The comparison of areal capacitances of LSG MSCs prepared using different laser powers at different current densities are shown in Figure 4F. The results show that areal capacitance decreases with increasing current density and applied laser power. The areal capacitances of LSG electrodes with increasing laser power are 17.0, 6.9, 5.2, 4.6, and 2.1 mF cm^{-2} , respectively, at a CD current density of 0.05 mA cm^{-2} . Thanks to the high areal capacitance and high conductivity of LSG

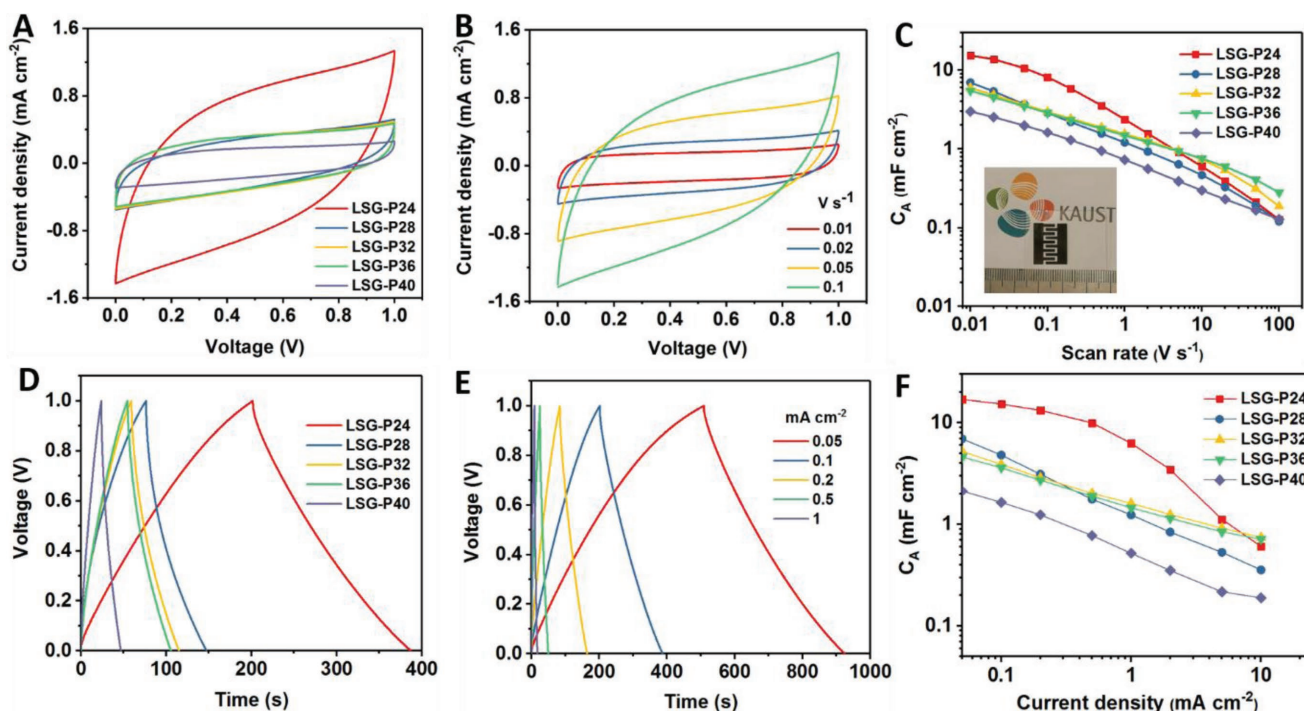


Figure 4. Electrochemical performances of MSCs fabricated using LSG electrodes in $\text{H}_2\text{SO}_4/\text{PVA}$ gel electrolyte. A) Cyclic voltammograms (measured at a scan rate 0.1 V s^{-1}) of MSCs with LSG electrodes prepared at different CO_2 laser powers. B) Cyclic voltammograms of MSCs fabricated with LSG-P24 electrodes measured at different scan rates. C) Areal capacitance versus scan rate for MSCs using LSG electrodes prepared at different CO_2 laser powers. D) The CD curves of MSCs using LSG electrodes prepared at different CO_2 laser powers, measured at charge-discharge current density of 0.1 mA cm^{-2} . E) The CD curves of MSCs using LSG-P24 electrodes prepared at different charge-discharge current densities. F) Areal capacitance versus current densities of MSCs fabricated using LSG electrodes prepared under different CO_2 laser powers. The inset of (C) is the digital photograph of LSG MSC.

electrodes, LSG MSCs possess good energy-power characteristics. Figure S15B,C in the Supporting Information shows both areal and volumetric energy and power densities of the MSCs using lignin-derived LSG electrodes prepared at different laser powers. It can be seen that LSG-P24 exhibits the highest areal energy density of $0.0026 \text{ mWh cm}^{-2}$ (Figure S15B, Supporting Information) corresponding to a volumetric energy density of $0.657 \text{ mWh cm}^{-3}$ (Figure S15C, Supporting Information). All MSCs show high areal power densities around $\approx 4 \text{ mW cm}^{-2}$, corresponding to a volumetric energy density of about $\approx 1000 \text{ mW cm}^{-3}$. Among them, LSG-P28 MSC displays the highest volumetric power density of 1987 mW cm^{-3} . Besides the good energy-power characteristics, LSG MSC shows stable cycling stability for over 12 000 cycles at a current density of 2 mA cm^{-2} , with a high capacitance retention of 99.2% (Figure S15D, Supporting Information).

The electrochemical performance of lignin-derived LSG MSCs was further enhanced by sputtering an Au coating the on top of LSG to increase the conductivity of the finger electrodes (see Figure 1). The direct sputtering of Au was done after the laser-scribing process over the entire substrate surface (Figure 1, step 3a). After the Au sputtering, a water lift-off process was used to wash away the Au coated lignin which had not been converted to LSG, resulting in the Au coated LSG electrodes (Figure S2F, Supporting Information). CVs of MSCs with Au/LSG electrodes are shown in Figure 5A,B. A scan rate of up to 500 V s^{-1} can be used while retaining a

reasonable looking C-V curve. One of the other key advantages of the Au coating is to increase the capacitance of the MSC at low charge-discharge rate. LSG-P36-Au possesses a high areal capacitance of 11.9 mF cm^{-2} at 0.02 mA cm^{-2} which is almost double that of uncoated LSG-P36 electrode (6.5 mF cm^{-2}). Remarkably, the LSG-P24-Au electrode displays a much higher capacitance of 25.1 mF cm^{-2} (6.27 F cm^{-3} , in Figure S16A, Supporting Information), compared with that of uncoated LSG-P24 (17.0 mF cm^{-2} , 4.25 F cm^{-3}) at a current density of 0.05 mA cm^{-2} . The increased capacitance with Au coating results from better charge carrier distribution in the horizontal direction of finger electrodes, which makes full utilization of the meso/microporous structure of LSG-P36. Although the capacitance at low current density increased, the capacitance at high current density decreased (Figure 5C), most likely because the Au coating can mainly cover the surface macropores of LSG electrode. As a result, the areal power density of LSG-P36 was greatly improved by Au coating, the highest power of LSG-P36 is 3.37 mW cm^{-2} , and the highest power for LSG-P36-Au is 5.79 mW cm^{-2} . LSG-P36-Au MSC also shows ultrastable cycling stability during 12 000 CD cycles, with a high capacitance retention of 98.5% (Figure 5D). The above results demonstrate that we can tune the electrochemical performances of MSC by tuning the conductivity of finger electrodes of MSC.

In addition, we have evaluated the volumetric energy and power density of the Au-coated electrodes. For example, the LSG-P24-Au electrode possesses a much higher volumetric

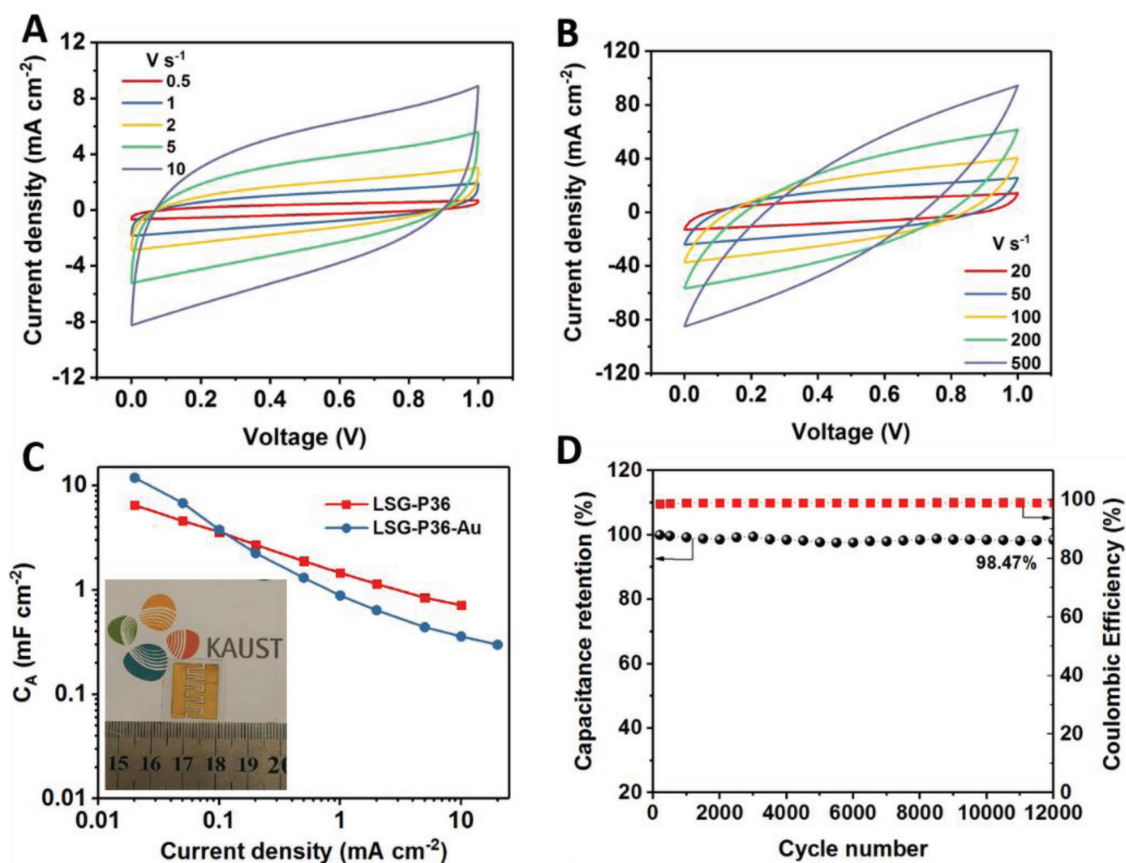


Figure 5. Electrochemical performance of MSCs fabricated using an Au/LSG finger electrode (LSG-P36-Au) in $\text{H}_2\text{SO}_4/\text{PVA}$ gel electrolyte. A,B) Cyclic voltammograms of LSG-P36-Au MSCs obtained at different scan rates. C) Dependence of the areal capacitances of LSG-P36 and LSG-P36-Au MSCs on charge–discharge current densities. D) Cycling stability of LSG-P36-Au MSC measured at a current density of 2 mA cm^{-2} . The inset of (C) is the digital photograph of LSG-P36-Au MSC.

energy density ($\approx 1.0 \text{ mWh cm}^{-3}$) compared with $0.657 \text{ mWh cm}^{-3}$ for LSG-P24. LSG-P24-Au delivers a high volumetric power density of $1704.5 \text{ mW cm}^{-3}$ compared with 641.7 mW cm^{-3} for LSG-P24 (Figure S16D, Supporting Information). The areal capacitance, volumetric capacitance, volumetric energy density, and volumetric power density of the LSG-P24-Au MSC are further compared with literature reports on MSCs based on laser-scribed graphene electrodes (Table S2, Supporting Information). It can be seen that the LSG-P24-Au MSC offers one of the highest volumetric capacitances and volumetric energy densities. The volumetric energy density of our LSG-P24-Au MSC is much higher than the laser-induced graphene (LIG) based MSC (0.2 mWh cm^{-3}),^[15] the carbon quantum dot derived graphene MSC (0.03 mWh cm^{-3}),^[46] and boron doped LIG-based MSC (5B-LIG-MSC, $\approx 0.6 \text{ mWh cm}^{-3}$).^[30] Actually, the volumetric energy density of LSG-P24-Au MSC is comparable to the LIG-based MSC using ionic liquid electrolyte (about 1 mWh cm^{-3}).^[15]

In summary, we have successfully prepared laser-scribed 3D hierarchical porous graphene electrodes from lignin films. A LLL technique has been developed to pattern microsupercapacitor (MSC) electrodes combined with simple water lift-off process. The lignin-derived LSG electrodes can be prepared on several substrates due to the unique water-soluble properties

of alkaline lignin in water. Further, we demonstrated that multilayer electrodes (e.g., Au/LSG) can be fabricated using this process. The MSCs fabricated using LLL exhibit high areal capacitance (25.1 mF cm^{-2}), high volumetric energy density ($\approx 1 \text{ mWh cm}^{-3}$), and high volumetric power density ($\approx 2 \text{ W cm}^{-3}$). The LLL method is a green and sustainable process, since it does not use toxic precursors or solvents. The versatility and environmental friendliness of lignin laser lithography can inspire both the fabrication of MSC, production of graphene and the sustainable utilization of lignin.

Experimental Section

Preparation of LSG-Based MSC: Lignin used in this work is alkaline lignin (471003, Sigma-Aldrich), which is water soluble and contains $\approx 4 \text{ wt\%}$ sulfur existing in the form of sodium sulfonate. Lignin (10 g) with PVA (average M_w 89 000, Sigma-Aldrich) (10 g) were mixed in deionized water (100 mL) while stirring in a 60°C oil bath for 4 h. The room-temperature lignin/PVA solution was used to prepare lignin/PVA films, using a blade coating technique, on ozone treated plastic substrates including PC, PMMA, and PET. PVA in the lignin/PVA film acts as a binder that fully decomposes during the laser scribing process. The thickness of dried lignin/PVA film was about $40 \mu\text{m}$. After drying in air to remove extra water for 24 h, the lignin/PVA film was used for the

laser scribing process. The Laser scribing process was conducted using a commercial CO₂ laser (10.6 μm) cutting machine (Universal X-660 laser cutter platform, Universal, Austria). The beam size of laser was about 100 μm. The peak laser power was 75 W and the full scan speed was 75 in. s⁻¹. Laser pulse was set at 1000 dpi in.⁻¹. The applied laser power was from 2.4% to 4.0% of the total laser power with an increment of 0.4%. The scan rate was set at 3% and laser beam was focused at a z distance of 3 mm. LSG prepared at a laser power of X% is denoted as LSG-P10X.

After laser scribing, the laser-scribed lignin/PVA composite film was put into deionized water to wash off the remaining lignin on plastic surface. The washed LSG was then put into a vacuum oven at 50 °C overnight to evaporate the remaining water. After drying, the LSG was assembled into an MSC with comb-like interdigitated electrodes. Silver paste was used to connect LSG and copper terminals and epoxy resin was used to separate the active electrodes and the silver paste (the assembly and dimension of LSG MSC is shown in Figure S1, Supporting Information). After assembly, the electrodes of MSC were coated with 1.0 mol L⁻¹ H₂SO₄/PVA gel electrolyte. Before electrochemical testing, the MSCs were placed in air overnight to make sure the gel electrolyte completely covered the LSG electrodes. 1.0 mol L⁻¹ H₂SO₄/PVA gel electrolyte was prepared by mixing H₂SO₄ (1.0 g) with H₂O (10 g) and PVA (1.0 g) at 80 °C until a clear gel formed.

General Characterization: The sheet resistance of LSG was measured using a four-point probe resistivity measurement system (RZ2001i, Ozawa Science Co Ltd, Nagoya, Japan). Thickness of all samples were measured by cross-section SEM. BET surface area and pore size distribution were evaluated by N₂ adsorption-desorption isotherms measured on an N₂ adsorption/desorption analyzer (ASAP 2420, Micrometrics, USA). Scanning electron microscopy (SEM) images were taken on a field emission scanning electron microscopy (Merlin, ZEISS, Germany) operated at 5 kV and 100 pA. Transmission electron microscopy (TEM) images were taken on transmission electron microscope (Titan 80-300 ST, FEI, Thermo Fisher Scientific). XRD patterns were collected on a Bruker diffractometer (D8 Advance) with Cu K_α radiation (λ = 1.5406 Å). Raman spectra were collected on a micro-Raman spectrometer (LabRAM ARAMIS, Horiba-Jobin Yvon, France) using a cobalt laser (473 nm). Thermogravimetric analysis (STA 449F1, NETZSCH, Germany) were measured within the temperature range from 30 to 900 °C at a heating rate 10 °C min⁻¹ in Ar atmosphere. XPS analysis was conducted on photoelectron spectrometer (Kratos Axis Supra, Shimadzu, Japan). The LSG samples for XRD, BET, TEM, and thermogravimetric analysis experiments were powders obtained from LSG films.

Raman spectra data were used to calculate the crystalline size along the *a* axis (*L_a*) from the ratio of the intensity of G peak and D peak, the *L_a* was calculated through the following equation

$$L_a = (2.4 \times 10^{-10}) \times \lambda_f^4 \times \left(\frac{I_D}{I_G}\right)^{-1} \quad (1)$$

Electrochemical Measurement and Calculation: CV and galvanostatic CD tests were conducted on a CHI660D electrochemical workstation (CHI Instruments, USA). All measurements were conducted in ambient conditions. The electrochemical impedance spectra of MSC were measured on a VMP3 electrochemical workstation at open circuit voltage with a sinusoidal voltage amplitude of 10 mV in the frequency range from 100 kHz to 10 mHz.

The areal specific capacitances based on the cyclic voltammograms were calculated by Equation (2).

$$C_A = \frac{\int i dV}{S \times \nu \times \Delta V} \quad (2)$$

where *S* is the active electrode area (cm²), with 0.5 cm² for the device configuration of this work. *ν* is the voltage scan rate (V s⁻¹), *ΔV* is the voltage range, and *i* is the current response in the CV scans. $\int i dV$ is the integrated area of the discharge portion of C–V curve.

The areal capacitance derived from CD curves was calculated via the following equation

$$C_A = \frac{2I \int V dt}{S(\Delta V)^2} \quad (3)$$

where *I* is the constant current in CD measurements. $\int V dt$ is the integrated area of the discharge branch of CD curves. *ΔV* is the voltage change during the discharge process. *ΔV* was calculated using the maximum voltage upon discharge, while subtracting the voltage drop during initial discharge.

The areal and volumetric energy densities and power densities were calculated based on the equations in reported in relevant reference [15].

Supporting Information

Supporting Information is available from the Wiley Online Library or from the author.

Acknowledgements

W.L.Z. and Y.J.L. contributed equally to this work. Research reported in this publication was supported by King Abdullah University of Science and Technology (KAUST). Authors thank the Advanced Nanofabrication, Imaging and Characterization Laboratory at KAUST for their excellent support. W.L.Z. thanks Fan Zhang and Dr. Chuan Xia at KAUST for their help.

Conflict of Interest

The authors declare no conflict of interest.

Keywords

graphene, laser scribing, lignin, lithography, microsupercapacitors

Received: June 13, 2018

Revised: July 18, 2018

Published online: August 9, 2018

- [1] M. Beidaghi, Y. Gogotsi, *Energy Environ. Sci.* **2014**, 7, 867.
- [2] N. A. Kyeremateng, T. Brousse, D. Pech, *Nat. Nanotechnol.* **2017**, 12, 7.
- [3] Q. Jiang, N. Kurra, C. Xia, H. N. Alshareef, *Adv. Energy Mater.* **2017**, 7, 1601257.
- [4] N. Kurra, B. Ahmed, Y. Gogotsi, H. N. Alshareef, *Adv. Energy Mater.* **2016**, 6, 1601372.
- [5] L. Li, E. B. Secor, K. S. Chen, J. Zhu, X. Liu, T. Z. Gao, J. W. T. Seo, Y. Zhao, M. C. Hersam, *Adv. Energy Mater.* **2016**, 6, 1600909.
- [6] S. S. Delekta, A. D. Smith, J. Li, M. Östling, *Nanoscale* **2017**, 9, 6998.
- [7] Z. Liu, Z. S. Wu, S. Yang, R. Dong, X. Feng, K. Müllen, *Adv. Mater.* **2016**, 28, 2217.
- [8] D. Pech, M. Brunet, P. L. Taberna, P. Simon, N. Fabre, F. Mesnilgrente, V. Conédéra, H. Durou, *J. Power Sources* **2010**, 195, 1266.
- [9] Y. G. Zhu, Y. Wang, Y. Shi, J. I. Wong, H. Y. Yang, *Nano Energy* **2014**, 3, 46.

- [10] X. Pu, M. Liu, L. Li, S. Han, X. Li, C. Jiang, C. Du, J. Luo, W. Hu, Z. L. Wang, *Adv. Energy Mater.* **2016**, 6, 1601254.
- [11] D. Pech, M. Brunet, H. Durou, P. Huang, V. Mochalin, Y. Gogotsi, P.-L. Taberna, P. Simon, *Nat. Nanotechnol.* **2010**, 5, 651.
- [12] L. Li, C. Fu, Z. Lou, S. Chen, W. Han, K. Jiang, D. Chen, G. Shen, *Nano Energy* **2017**, 41, 261.
- [13] N. Kurra, Q. Jiang, H. N. Alshareef, *Nano Energy* **2015**, 16, 1.
- [14] M. F. El-Kady, V. Strong, S. Dubin, R. B. Kaner, *Science* **2012**, 335, 1326.
- [15] J. Lin, Z. Peng, Y. Liu, F. Ruiz-Zepeda, R. Ye, E. L. G. Samuel, M. J. Yacamán, B. I. Yakobson, J. M. Tour, *Nat. Commun.* **2014**, 5, 5714.
- [16] Z. Wan, E. W. Streed, M. Lobino, S. Wang, R. T. Sang, I. S. Cole, D. V. Thiel, Q. Li, *Adv. Mater. Technol.* **2018**, 3, 1700315.
- [17] M. F. El-Kady, R. B. Kaner, *ACS Nano* **2014**, 8, 8725.
- [18] M. I. Serna, S. H. Yoo, S. Moreno, Y. Xi, J. P. Oviedo, H. Choi, H. N. Alshareef, M. J. Kim, M. Minary-Jolandan, M. A. Quevedo-Lopez, *ACS Nano* **2016**, 10, 6054.
- [19] J. Yeo, G. Kim, S. Hong, M. S. Kim, D. Kim, J. Lee, H. B. Lee, J. Kwon, Y. D. Suh, H. W. Kang, H. J. Sung, J. H. Choi, W. H. Hong, J. M. Ko, S. H. Lee, S. H. Choa, S. H. Ko, *J. Power Sources* **2014**, 246, 562.
- [20] J. Y. Hwang, M. Li, M. F. El-Kady, R. B. Kaner, *Adv. Funct. Mater.* **2017**, 27, 1605745.
- [21] P. Yadav, A. Basu, A. Suryawanshi, O. Game, S. Ogale, *Adv. Mater. Interfaces* **2016**, 3, 1600057.
- [22] H. Lee, S. Hong, J. Kwon, Y. D. Suh, J. Lee, H. Moon, J. Yeo, S. H. Ko, *J. Mater. Chem. A* **2015**, 3, 8339.
- [23] L. X. Duy, Z. Peng, Y. Li, J. Zhang, Y. Ji, J. M. Tour, *Carbon* **2017**, 126, 472.
- [24] W. Gao, N. Singh, L. Song, Z. Liu, A. L. M. Reddy, L. Ci, R. Vajtai, Q. Zhang, B. Wei, P. M. Ajayan, *Nat. Nanotechnol.* **2011**, 6, 496.
- [25] F. Clerici, M. Fontana, S. Bianco, M. Serrapede, F. Perrucci, S. Ferrero, E. Tresso, A. Lamberti, *ACS Appl. Mater. Interfaces* **2016**, 8, 10459.
- [26] A. Lamberti, F. Clerici, M. Fontana, L. Scaltrito, *Adv. Energy Mater.* **2016**, 6, 1600050.
- [27] L. Li, J. Zhang, Z. Peng, Y. Li, C. Gao, Y. Ji, R. Ye, N. D. Kim, Q. Zhong, Y. Yang, H. Fei, G. Ruan, J. M. Tour, *Adv. Mater.* **2016**, 28, 838.
- [28] Z. Peng, J. Lin, R. Ye, E. L. G. Samuel, J. M. Tour, *ACS Appl. Mater. Interfaces* **2015**, 7, 3414.
- [29] Y. Li, D. X. Luong, J. Zhang, Y. R. Tarkunde, C. Kittrell, F. Sargunraj, Y. Ji, C. J. Arnusch, J. M. Tour, *Adv. Mater.* **2017**, 29, 1700496.
- [30] Z. Peng, R. Ye, J. A. Mann, D. Zakhidov, Y. Li, P. R. Smalley, J. Lin, J. M. Tour, *ACS Nano* **2015**, 9, 5868.
- [31] P. Nayak, Q. Jiang, N. Kurra, X. Wang, U. Buttner, H. N. Alshareef, *J. Mater. Chem. A* **2017**, 5, 20422.
- [32] J. Zhang, C. Zhang, J. Sha, H. Fei, Y. Li, J. M. Tour, *ACS Appl. Mater. Interfaces* **2017**, 9, 26840.
- [33] R. Ye, Z. Peng, T. Wang, Y. Xu, J. Zhang, Y. Li, L. G. Nilewski, J. Lin, J. M. Tour, *ACS Nano* **2015**, 9, 9244.
- [34] P. Nayak, N. Kurra, C. Xia, H. N. Alshareef, *Adv. Electron. Mater.* **2016**, 2, 1600185.
- [35] L. Q. Tao, H. Tian, Y. Liu, Z. Y. Ju, Y. Pang, Y. Q. Chen, D. Y. Wang, X. G. Tian, J. C. Yan, N. Q. Deng, Y. Yang, T. L. Ren, *Nat. Commun.* **2017**, 8, 14579.
- [36] S. Luo, P. T. Hoang, T. Liu, *Carbon* **2016**, 96, 522.
- [37] S. P. Singh, Y. Li, J. Zhang, J. M. Tour, C. J. Arnusch, *ACS Nano* **2018**, 12, 289.
- [38] S. P. Singh, Y. Li, A. Be'Er, Y. Oren, J. M. Tour, C. J. Arnusch, *ACS Appl. Mater. Interfaces* **2017**, 9, 18238.
- [39] R. Ye, Y. Chyan, J. Zhang, Y. Li, X. Han, C. Kittrell, J. M. Tour, *Adv. Mater.* **2017**, 29, 1702211.
- [40] Y. Chyan, R. Ye, Y. Li, S. P. Singh, C. J. Arnusch, J. M. Tour, *ACS Nano* **2018**, 12, 2176.
- [41] A. J. Ragauskas, G. T. Beckham, M. J. Biddy, R. Chandra, F. Chen, M. F. Davis, B. H. Davison, R. A. Dixon, P. Gilna, M. Keller, P. Langan, A. K. Naskar, J. N. Saddler, T. J. Tschaplinski, G. A. Tuskan, C. E. Wyman, *Science* **2014**, 344, 1246843.
- [42] M. P. Pandey, C. S. Kim, *Chem. Eng. Technol.* **2011**, 34, 29.
- [43] Y. Li, Y.-S. Hu, H. Li, L. Chen, X. Huang, *J. Mater. Chem. A* **2016**, 4, 96.
- [44] W. Zhang, H. Lin, Z. Lin, J. Yin, H. Lu, D. Liu, M. Zhao, *ChemSusChem* **2015**, 8, 2114.
- [45] X. Xu, J. Zhou, D. H. Nagaraju, L. Jiang, V. R. Marinov, G. Lubineau, H. N. Alshareef, M. Oh, *Adv. Funct. Mater.* **2015**, 25, 3193.
- [46] V. Strauss, C. Marsh, M. Kowal, M. F. El-Kady, R. B. Kaner, *Adv. Mater.* **2018**, 30, 1704449.
- [47] A. C. Ferrari, J. C. Meyer, V. Scardaci, C. Casiraghi, M. Lazzeri, F. Mauri, S. Piscanec, D. Jiang, K. S. Novoselov, S. Roth, A. K. Geim, *Phys. Rev. Lett.* **2006**, 97, 187401.